JOURNAL OF SYNCHROTRON RADIATION
ISSN 1600-5775

New high-throughput endstation to accelerate the experimental optimization pipeline for synchrotron X-ray footprinting

Rohit Jain,[a,b,c] Donald Abel,[a,d] Maksim Rakitin,[d] Michael Sullivan,[a,c] David T. Lodowski,[b,c] Mark R. Chance[a,b,c]* and Erik R. Farquhar[a,c]*

[a]Center for Synchrotron Biosciences, Case Western Reserve University, School of Medicine, 10900 Euclid Avenue, Cleveland, OH 44106, USA, [b]Center for Proteomics and Bioinformatics, Case Western Reserve University, School of Medicine, 10900 Euclid Avenue, Cleveland, OH 44106, USA, [c]Department of Nutrition, Case Western Reserve University, School of Medicine, 10900 Euclid Avenue, Cleveland, OH 44106, USA, and [d]National Synchrotron Light Source II, Brookhaven National Laboratory, Upton, NY 11973, USA. *Correspondence e-mail: mrc16@case.edu, efarquhar@bnl.gov

Received 1 February 2021
Accepted 11 May 2021

Edited by E. F. Garman, University of Oxford, United Kingdom

Keywords: X-ray radiolysis; high throughput; macromolecular dynamics; nucleic acids; protein structure; hydroxyl radical footprinting; *Bluesky*.

Supporting information: this article has supporting information at journals.iucr.org/s

Synchrotron X-ray footprinting (XF) is a growing structural biology technique that leverages radiation-induced chemical modifications via X-ray radiolysis of water to produce hydroxyl radicals that probe changes in macromolecular structure and dynamics in solution states of interest. The X-ray Footprinting of Biological Materials (XFP) beamline at the National Synchrotron Light Source II provides the structural biology community with access to instrumentation and expert support in the XF method, and is also a platform for development of new technological capabilities in this field. The design and implementation of a new high-throughput endstation device based around use of a 96-well PCR plate form factor and supporting diagnostic instrumentation for synchrotron XF is described. This development enables a pipeline for rapid comprehensive screening of the influence of sample chemistry on hydroxyl radical dose using a convenient fluorescent assay, illustrated here with a study of 26 organic compounds. The new high-throughput endstation device and sample evaluation pipeline now available at the XFP beamline provide the worldwide structural biology community with a robust resource for carrying out well optimized synchrotron XF studies of challenging biological systems with complex sample compositions.

1. Introduction

Synchrotron X-ray footprinting (XF) is an increasingly prominent and valuable structural biology method used to probe the structure and dynamics of biological macromolecules and their interactions with molecules such as drug candidates in native solution states. Beyond these widespread applications, XF can probe macromolecular structures on surfaces and in intact cell or viral contexts (Kiselar & Chance, 2018; Chance *et al.*, 2020). The method uses ionizing broadband X-ray radiation from a synchrotron to promote the radiolysis of water, generating short-lived hydroxyl radicals that rapidly react with biomolecules and other components of a solution in their immediate vicinity. For proteins, hydroxyl radicals attack solvent-accessible amino acid side chains leading to an oxidative covalent modification of the side chain that can be detected using mass spectrometry (MS) based readout methods that probe for well documented amino acid mass changes (Xu & Chance, 2007). Bulk solvent-inaccessible regions of proteins, such as buried hydrophobic core areas or membrane-associated regions, show little to no covalent modifications, while those parts of a protein in contact with


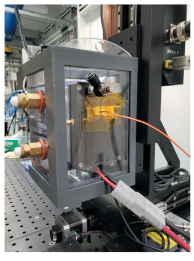

bulk water (and even internal structural waters) can be covalently labeled. In the case of nucleic acids, hydroxyl radicals readily cleave the phosphodiester backbone, again in a solvent-accessibility mediated fashion that relies on the specific conformation and molecular contacts of the nucleic acid backbone. Following X-ray exposure, nucleic acid XF samples are analyzed using gel electrophoresis or sequencing as readouts to identify regions that are not cleaved due to protection from solvents. The inherent power of synchrotron XF lies in its ability to uncover changes in solvent accessibility as a function of a biomolecule's state in the native solution state, with minimal to no perturbation of the sample due to chemical treatment or a change in state like crystallization or vitrification. The most common approaches consist of pairwise comparisons in which one state of a biomolecule is examined by footprinting, and then a ligand, biomolecule binding partner, mutation or other perturbation is introduced and the readouts of the two states are examined for specific structural changes. Binding or folding events can lead to changes in the solvent accessibility of different regions of the target biomolecule, thus altering the rate and extent of reaction with hydroxyl radicals. These changes in reactivity can be correlated to the altered protection of a region due to the direct binding of a ligand or a change in the folded conformation like an allosteric change. Synchrotron XF has been applied to numerous biomedically important structural biology problems, including *in vitro* RNA folding (Sclavi *et al.*, 1998), ligand/drug binding (Sangodkar *et al.*, 2017), antibody epitope mapping (Deperalta *et al.*, 2013), identification of bound water networks within membrane proteins (Angel *et al.*, 2009; Gupta *et al.*, 2012) and many others. Furthermore, the method is not limited to steady-state conditions, as time-resolved approaches over a range of timescales can provide unique insights that are not obtainable by other synchrotron methods such as crystallography, cryo-EM or X-ray solution scattering. Pertinent examples include studies investigating how G-protein-coupled receptors (GPCRs) select for and bind their target G proteins (Du *et al.*, 2019), the folding pathway of ribosomal RNAs under *in vivo* conditions (Clatterbuck Soper *et al.*, 2013), and mechanisms of Zn transport (Gupta *et al.*, 2014*b*). Recent developments demonstrate that XF can also be employed as an absolute structure prediction tool through a workflow that integrates XF and computational modeling along with data from other biophysical methods such as crystallography, cryo-EM, small-angle X-ray scattering and nuclear magnetic resonance, as recently illustrated by the determination of the structure of a human estrogen receptor (Huang *et al.*, 2018). Synchrotron XF can therefore be used as a key component of a suite of integrated synchrotron-based structure-determination tools that can be deployed for a wide variety of biomedically relevant structure–function problems (Chance *et al.*, 2020).

The key element to successfully applying synchrotron XF to a research problem involves the delivery of a carefully controlled X-ray dose to the sample that strikes a balance in the level of radiation-induced modification to the sample, such that sufficient protein covalent labeling or nucleic acid backbone cleavage occurs to permit accurate quantification, while avoiding X-ray doses that lead to over-oxidation or indeed wholescale destruction of the sample. Hydroxyl radicals generated by X-ray radiolysis readily react with components of a sample beyond the target biomolecule(s), including buffers, buffer constituents or molecular oxygen, leading to undesirable secondary radical reactions and reduction of the total hydroxyl radical concentration available for reaction with the biomolecule(s) of interest. A thorough understanding of the effects and influence of the sample matrix as well as fully characterized, flexible, and reliable beamline instrumentation are essential for constructive results. To this end, we recently described the design and capabilities of the X-ray Footprinting of Biological Materials (XFP) beamline located at the National Synchrotron Light Source II (NSLS-II, Brookhaven National Laboratory, New York, USA), which was developed to provide access to the synchrotron XF technology for the structural biology research community (Asuru *et al.*, 2019).

The XFP beamline can deliver *ca.* 10^{16} photons s^{-1} (∼70 W power) of pink-beam X-ray radiation over a 4.5–16 keV energy range to two experimental endstations that differ in their achievable flux density and thus X-ray dose (Asuru *et al.*, 2019). The first endstation uses a capillary flow device to flow samples through the X-ray beam, with focused beam sizes as small as 120 µm × 450 µm [full width at half-maximum (FWHM), V × H], capable of delivering up to 500 W mm^{-2} power densities to the sample (at 500 mA NSLS-II ring current). This endstation enables XF of highly scavenging systems such as membrane proteins, live cells or mega-Dalton-sized protein complexes, with microsecond-scale X-ray exposures having a very high concentration of hydroxyl radicals to overcome these sample matrix effects. The second endstation provides a larger defocused X-ray beam that is typically 2.6 mm × 2.6 mm to 3.0 mm × 3.0 mm in size (FWHM, V × H); the 5–10 W mm^{-2} power densities available with this beam-size condition are well suited for studying less scavenging biological systems under steady-state conditions such as smaller soluble proteins, as well as freeze-quench samples prepared in advance. For this endstation, the standard sample format consists of 5 µl sample droplets held by surface tension on the bottom of 200 µl PCR tubes, producing a 2.5 mm-diameter droplet well matched to the X-ray beam size, along with a sample depth of *ca.* 1 to 1.5 mm that provides good energy deposition into aqueous solutions over the 4.5–16 keV energy range of the XFP beamline. The initial defocused endstation instrument was a multi-sample holder (MSH) device, originally developed at NSLS X28C, that held up to 23 individual PCR tubes and was outfitted with Peltier coolers for exposure of frozen samples at temperatures as low as −30°C (Hao *et al.*, 2018). This apparatus proved popular with the XFP beamline user community during early user operations for both scientific and technical reasons, as it allowed fairly rapid exposure of large numbers of samples while avoiding some of the challenges associated with work at the high-dose endstation such as capillary damage by the high-flux density X-ray beam. However, limitations of the MSH as a workhorse

synchrotron XF device also became increasingly apparent as it was somewhat challenging to reproducibly align and had looser-than-desired mechanical tolerances that required careful manual loading of individual PCR tubes to ensure consistent exposures from run to run. There was clear scope for a new apparatus with greater throughput and improved automation that would allow experimenters to focus more of their energies and limited beam time on science problems and sample handling and less on operation of beamline equipment.

This article reports the design and implementation of a new apparatus for high-throughput synchrotron XF based around the SBS 96-well PCR microplate format, as well as supporting diagnostic instrumentation to image the X-ray beam and monitor experiment reliability. This new device enables a fast screening pipeline for characterization of the influence of sample constituents on hydroxyl radical dose, thus enabling faster and more complete experimental optimization prior to conducting X-ray exposures for subsequent mass spectrometric or sequencing analysis. Herein, we demonstrate the utility of this new endstation device, employing it to examine the influence on X-ray generated hydroxyl-radical dose of 26 different reagents commonly encountered in biochemical research, providing experimental design guidance to the synchrotron XF user community.

2. High-throughput footprinting endstation

2.1. Well high-throughput device

We identified two design objectives when we set out to develop the new high-throughput XF apparatus for the XFP beamline. First, we sought to increase the number of samples that could be exposed in a single set of experiments beyond the 23 individual 200 µl PCR tubes possible in the original MSH device. A 96-well PCR plate format (ThermoFisher AB0600) comprising an 8 by 12 array of 200 µl PCR tubes was selected as the basis of the new design, due the ubiquity of this format and availability of 8- and 12-tube PCR strips. This format has the added benefit of reducing sample handling and risks of error in loading samples, and is more amenable to shipping samples both to and from the beamline for exposure, compared with the use of individual PCR tubes. Secondly, we also sought to improve sample cooling through improved thermal contact with the sample, to reduce undesired modification of samples due to local beam-induced heating during exposure. While the original MSH device could achieve temperatures as low as −30°C via Peltier cooling, the individual wells for each PCR tube were straight bored holes, thus limiting the fraction of the tapered PCR tube that was in (thermal) contact with cooled metal.

The new assembly, shown in Fig. 1, consists of a water block with connections to a recirculating chiller for cooling, a cold plate/Peltier cooler assembly and the sample block. The sample block, machined from oxygen-free copper, was designed to match the tapered contours of the individual PCR tubes in order to maximize thermal contact and ensure precise and reproducible alignment of samples. A type-K thermocouple is mounted to the interior of the sample block for readouts of the sample temperature. This block is in thermal contact with a second oxygen-free copper cooling plate, which functions to secure the Peltier modules in place between the sample and the water block. During the development of this device, we initially used two two-stage Peltier modules (Custom Thermoelectric 25412-5L31-07CQQ) for cooling. However, we observed long cool-down times (>2 h) and a slow recovery to the desired base temperature when samples were loaded. We improved cooling capacity in the final design by adding another single-stage Peltier module (Custom Thermoelectric 19911-5P31-15CQ) that acts to cool the two-stage modules during operation, providing a lower ultimate base temperature and more rapid cooldown. Finally, the water block, machined from aluminium, functions to keep the Peltier modules cool during their operation, as well as to secure the assembly to the motion stage. The recirculating water circuit was designed to maximize thermal contact and throughput,

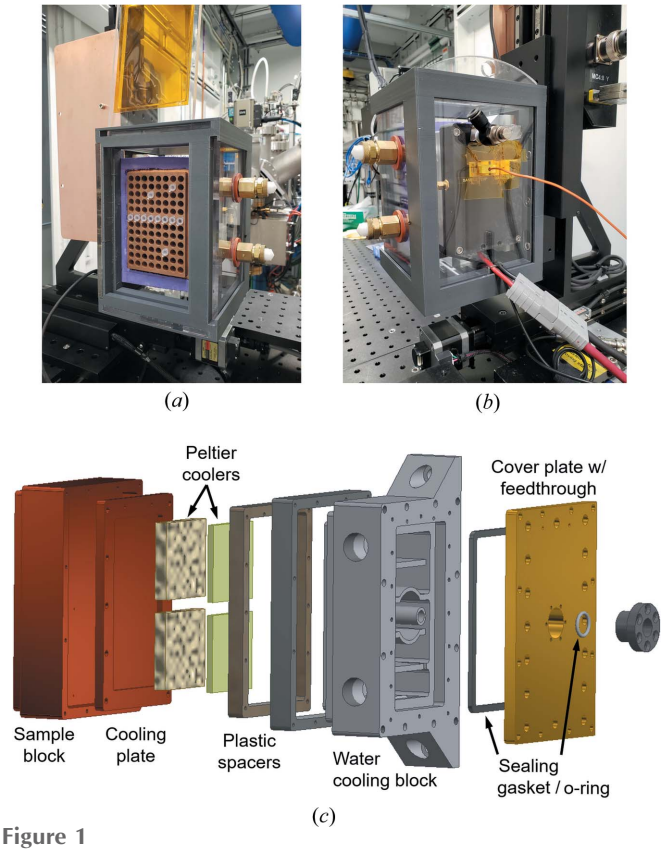

Figure 1
Photographs of the front (*a*) and rear (*b*) of the 96-well high-throughput apparatus mounted on a two-axis motion stage. In the front view, PCR tubes are shown installed into the copper sample block, with purple insulating material around the edges of the block to minimize heat absorption from the environment when the block is being cooled. The Kapton window for the front exposure side of the device is removable to facilitate sample loading and unloading. The rear panel of the unit (*b*) includes a nitrogen gas port, thermocouple connectors and the DC power connector for the Peltier coolers. Panel (*c*) shows an exploded view of the internal layers of the device to illustrate the assembly, in which the sample block that holds the 96 PCR tubes is stacked on top of a cooling plate that is in thermal contact with the Peltier coolers. These coolers are in turn attached to a water-cooling block for heat removal during Peltier operation.

thereby increasing the achievable cooling capacity of the Peltier modules. The water block includes a feedthrough for Peltier module power and thermocouple wires to the outside of the unit. Plastic spacer pieces seal the interior of the unit and minimize thermal shorts between the water and sample blocks when the system is running at low temperatures. A 1.0 mm-diameter fixed aperture at two sample positions (corresponding to the F1 and C1 cells of the 96-well PCR plate) passes through all components of the assembly, which facilitates alignment of the assembly and sample cells to the X-ray beam using a 10 mm × 20 mm PIN diode (OSI Optoelectronics) connected to an electrometer for current readback (*vide infra*).

The entire high temperature (HT) assembly is aligned to the X-ray beam using a custom two-axis stepper-motor-driven stage with 200 mm travel on both axes (American Linear Manufacturers). Both stage axes are outfitted with 1.0 mm-pitch lead screws and incremental linear encoders (Renishaw, 100 nm resolution) to provide precise and reproducible positioning, with motion control provided by DeltaTau GeoBrick LV controllers. The assembly is mounted to the vertical axis of the stage with a thermally isolating G10 block placed between the water-cooling block and stage. A plastic box with polycarbonate windows encloses the entire assembly and is intended to reduce ice accumulation through a slow flow of inert nitrogen purge gas during sustained low-temperature operation (the front window facing X-ray beam instead uses 50 µm-thick Kapton film as the window material). It also provides secondary containment for samples requiring biosafety level 2 (BSL-2) controls, such as viruses or prion-type aggregates. In our hands, this design reliably achieves and maintains sample temperatures as low as −40°C for XF of frozen samples, with cool-down from room temperature complete in less than 60 minutes. It can also be operated at temperatures spanning +4 to +37°C via direct cooling or heating (as appropriate) using the recirculating chiller without powering the Peltier coolers.

2.2. Modular beam diagnostics and shutter system

The XFP beamline terminates in a 100 µm-thick 10 mm-diameter diamond exit window mounted in a 4.5 inch ConFlat (CF) flange. Initially this exit window was protected from inadvertent damage by a plastic cover outfitted with a nitrogen gas purge (to minimize ozone formation that damages the diamond) and a slot to manually install aluminium attenuators to control total photon flux on the sample. The development of the new 96-well apparatus offered an opportunity to enhance automation and introduce several diagnostic tools to monitor the X-ray beam position and experimental reliability. We designed a modular system comprised of interchangeable parts that allow us to remotely control beam intensity through attenuators, monitor beam size and position, and operate and monitor the performance of a Uniblitz fast shutter (Fig. 2). The entire X-ray beam path in this assembly is helium purged to minimize undesired X-ray attenuation past the exit window.

The first component after the exit window is an aluminium wheel with eight slots containing seven aluminium foils of differing thickness; currently 25, 76, 152, 203, 305, 508 and 762 µm thicknesses are installed and the eighth position is open for the delivery of unattenuated beam. Movement of the wheel is controlled by a stepper motor connected via a belt.

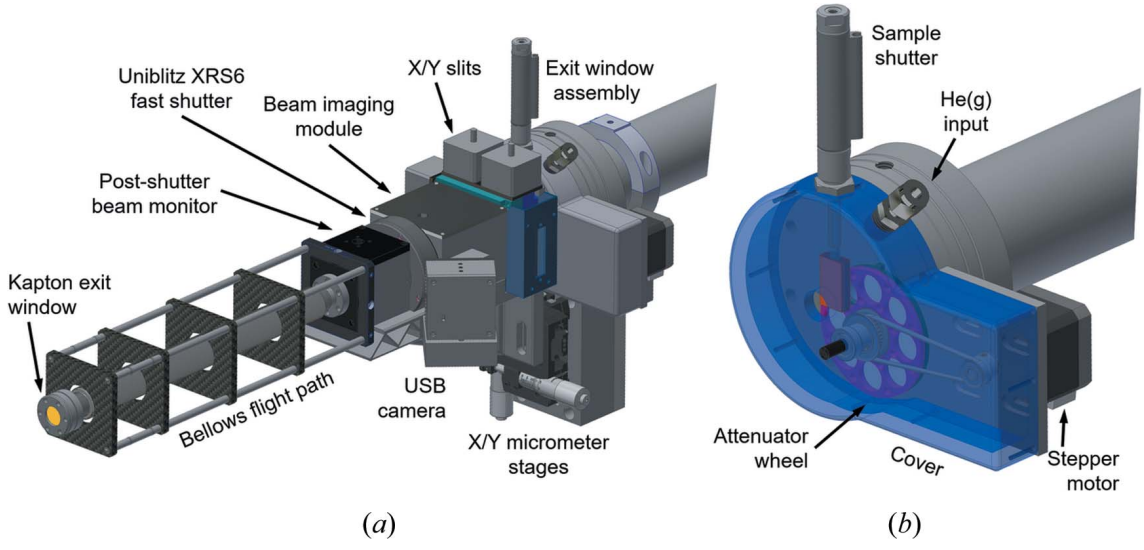

Figure 2
(*a*) An overview of the assembly that provides X-ray beam attenuation, images the X-ray beam and supports the Uniblitz fast shutter for the high-throughput endstation (the beam direction is from right to left). The assembly is shown mounted on the beamline's exit-window beampipe via a split-clamp assembly. Two micrometer stages allow manual alignment of the assembly into the X-ray beam after installation, with individual modules pre-aligned on a rail and a metal bellows flight path supported by a cage frame. The entire assembly is maintained under an He atmosphere, and surfaces between individual modules are sealed with O rings or directly screwed into one another to minimize gas leakage. Part (*b*) shows an expanded view of the exit-window assembly that directly attaches to the 4.5 inch CF flange containing the beamline's diamond exit window. The protective cover is shown as translucent blue. Inside, an eight-position attenuator wheel is connected via a belt to a stepper motor for positioning. A pneumatic solenoid drives a copper slug that serves as a sample shutter (shown in the down position). The interior environment is purged with He to reduce X-ray attenuation and minimize damage to the diamond window from ozone production.

This device enables remote selection of the level of X-ray attenuation without needing to enter the experimental hutch, allowing experimenters to examine a range of X-ray fluxes (and thus hydroxyl radical yields) in a single exposure series with the 96-well apparatus (Fig. S1 of the supporting information depicts flux curves for XFP as a function of attenuation, while Table S1 of the supporting information tabulates calculated beam powers). Just downstream is a sample shutter composed of a 0.5 inch-thick copper slug whose position is controlled by a pneumatic solenoid with independent open- and closed-position switches. Both the filter wheel and the sample shutter are enclosed within an assembly that attaches directly to the 4.5 inch CF flange of the exit window and provides a mount for the filter-wheel stepper motor while pre-aligning the filter wheel into the X-ray beam. An aluminium cover with an He gas inlet and an exit window for the X-ray beam encloses the filter-wheel assembly, protects the beamline exit window and allows efficient purging with He [Fig. 2(*b*)].

Subsequent components in the system [Figs. 2(*a*) and S2] are modular pieces mounted on a solid block, all of which are 3D printed in carbon fiber filled nylon (Markforged Onyx) to minimize weight. The support block attaches directly to the beampipe just upstream of the exit window through an aluminium split clamp. Two micrometer stages (Thorlabs XRN25P) allow for adjustment and alignment to the X-ray beam of the entire pre-aligned assembly in both the *X* and *Y* planes. Immediately after the filter-wheel/exit-window cover is a set of motorized X-ray slits (ADC SLT-100-P) with four independent blades that are used to reduce scatter and can be used as a beam-defining aperture at high attenuations where beam power is comparatively low (the slits are not water cooled). Both the upstream and downstream surfaces of the slit body are sealed to their respective mating surfaces with O rings to minimize He gas loss. Following the slits is a beam-imaging module used for real-time visualization of the X-ray beam using a diamond screen and camera. Specifically, a 100 µm-thick 12 mm-diameter nitrogen-doped optical-grade diamond (Applied Diamond) is mounted 45° to the X-ray beam. When struck by the pink X-ray beam, the diamond shows visible light fluorescence, the intensity of which is proportional to photon flux. We have tested several different grades of diamond (optical, thermal and tool grades) and dopants (nitrogen and boron) and have found that nitrogen-doped optical-grade diamond provides an ideal balance between optical clarity and fluorescence intensity with the pink X-ray beam available at the XFP beamline. The diamond screen is imaged (10 mm^2 field of view) using a compact USB camera (E-Con Systems See3Cam_CU55) controlled via a USB video class (UVC) driver available in the *EPICS areaDetector* package (https://github.com/areaDetector/ADUVC; Wlodek & Gofron, 2019). This provides a real-time visualization of beam intensity, size and position, providing an empirical measure of beam stability to the end user during experiments (Fig. S3).

Just downstream of the beam-imaging assembly is a Uniblitz XRS6 fast shutter (Vincent Associates), which we have carried over from the earlier MSH endstation. This shutter is used to define exposure time on the sample and operates reliably for exposure times greater than 10 ms. It is driven by a computer-controlled DG535 delay generator (Stanford Research Systems) that sends a square-wave pulse of desired duration to the VMM-T1 shutter driver connected to the shutter. We have introduced two new tools to monitor shutter function and reliability. First, we monitor the output of the shutter's internal electronic synchronization system, which provides a +5 V DC feedback signal that is sensitive to whether the fast shutter is greater than 80% open. This signal is read out using the beamline's Distributed I/O for Dynamic Equipment (DIODE) (Maytan & Derbenev, 2021) system as an *EPICS* process variable in microsecond units for each actuation of the shutter. This feature permits direct measurement of the actual open time of the fast shutter hence allowing correction for differences from the commanded opening time given to the delay generator, as well as a way to monitor degradation in shutter performance over time. In addition, in a module downstream of the Uniblitz shutter, a 10 mm × 20 mm PIN diode is mounted above and parallel to the X-ray beam and detects X-ray scatter in the He environment when the Uniblitz shutter is in the open state. Current produced by scattered X-rays on the diode is read by an electrometer, providing a second measure of shutter actuation and opening time, while also showing sensitivity to beam intensity due to attenuation provided by the upstream filter wheel.

The final component of the system consists of a flexible metal bellows assembly with 1-1/3 inch CF flanges on each end that can be compressed or extended depending on the position of the HT device to maximize the length of the He flight path. The bellows permanently attach to the beam-indicator module and are enclosed within a cage system (Thorlabs) for structural support and alignment. The downstream end terminates in a 25 µm-thick Kapton window mounted in a custom exit piece, which has an inlet for He gas supply that allows the entire beam flight path to be purged with He from both ends simultaneously.

2.3. Experiment control and data collection

All components of the high-throughput footprinting endstation are controlled via *EPICS* input–output controllers, as is standard at NSLS-II. *Control System Studio*, an *Eclipse*-based graphical user interface (GUI), is used for visualizing camera output, manual control of motion stages and presentation of output monitors such as the Uniblitz shutter opening times to the end user. Control of the HT apparatus for experimental work by users is implemented in the *Bluesky/Ophyd/Databroker* ecosystem deployed at NSLS-II (Allan *et al.*, 2019). In order to effectively manage workflow and present a simple easy-to-use user interface to the XFP user community, a *PyQt5* GUI application, shown in Fig. 3(*a*), has been developed that presents the user with a visual view of the 96-well array (Python code is available at https://github.com/NSLS-II-XFP/profile_collection). Within the GUI, each array

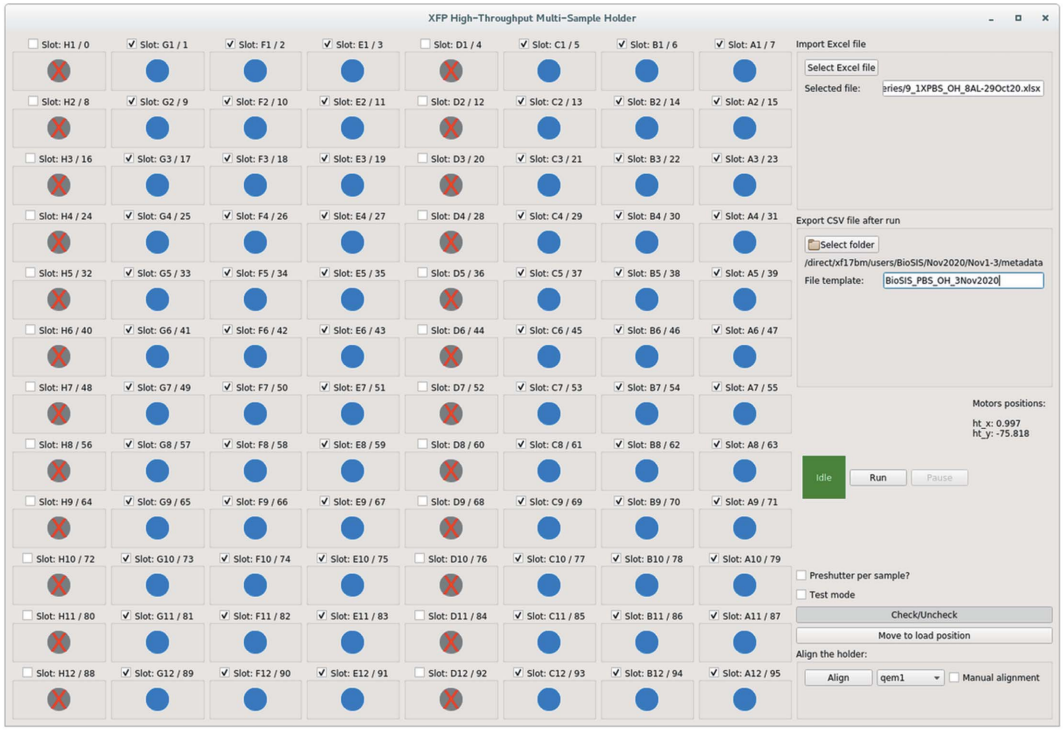

(*a*)

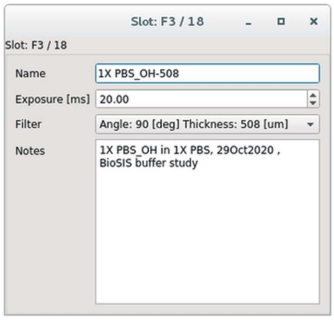

(*b*)

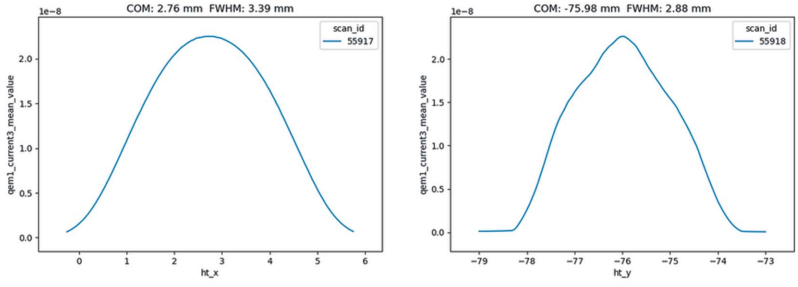

(*c*)

Figure 3
Screenshots of the *PyQt5* GUI application for a high-throughput footprinting experiment. The main screen is shown in (*a*) and depicts the layout of the 96-well array, with cells that have a blue circle selected for exposure. Clicking on a specific cell brings up the screen shown in (*b*) that allows the user to enter a sample name, exposure time, notes, and select an attenuation from a drop-down menu. The right side of the GUI application contains a series of interactive controls that allow the user to select an Excel file containing the experimental plan and output a CSV file with metadata, control data collection, and carry out automated alignment of the device. A typical alignment scan is shown in part (*c*) with the *x*-axis scan on the left and the *y*-axis scan on the right, with the automatically calculated center of mass (COM) and FWHM for each peak shown at the top of the respective plots. The differences in shape reflect the morphology of the X-ray beam.

position can be independently selected for exposure, with metadata input fields available for sample name or ID, exposure time, attenuation (limited to the eight values available on the filter wheel) and notes [Fig. 3(*b*)]. In addition, the GUI provides users with visual status indicators to show whether a sample position is active: where positions selected for exposure are flagged in blue, the next cell to be exposed is shown in red and exposed positions are colored green. To reduce the data-entry burden, the GUI accepts Excel spreadsheets tabulating sample names, exposure time, attenuation and notes for each position. This feature allows users to define sample exposure plans in advance, reducing the risk of mistakes and facilitating a mail-in program in which beamline staff can carry out exposures for remote users. After each exposure series, a CSV file can be written that contains selected metadata for each exposure, including a unique run identifier (version 4 UUID) assigned to the experiment by the *Bluesky* RunEngine that can be queried for additional metadata from *Databroker*. The GUI also provides a simple one-button automated alignment of the 96-well HT array, in which the HT apparatus is moved to one of the 1 mm alignment holes in the device and line scans are carried out in the *X* and *Y* axes using the current readout from the alignment PIN diode mounted behind the opening [Fig. 3(*c*)]. The centroid of each alignment scan is automatically determined and is used to generate a coordinate-lookup table for each position of the 96-

well sample array from the 9 mm × 9 mm separation between individual tubes in a standard PCR plate or strip.

In a typical experiment, *Bluesky* uses the coordinate-lookup table to move the HT device *X*/*Y* stages to a selected sample position, moves the filter wheel (if needed) to a selected attenuation, then actuates the Uniblitz fast shutter for the desired exposure time before moving to the next selected sample. The sample shutter can be actuated for each sample position to protect the Uniblitz shutter from extended pink-beam exposure or can remain open for the entire run. At typical 10–30 ms exposure times, an entire 96-well PCR plate is completed within *ca.* 5.5 minutes, not including the time to interlock or access the experimental hutch.

3. An HT pipeline for optimizing the XF experiment

3.1. Alexa488 dose-response assay and supporting equipment

We have previously described an Alexa488 fluorophore dose-response reporter assay, in which loss of Alexa488 fluorescence due to destruction of the fluorophore correlates to total hydroxyl radical dose as defined by the exposure time and X-ray flux (Gupta *et al.*, 2007). Assays with other hydroxyl radical dose reagents such as adenine have also been developed (Xie & Sharp, 2015). Regardless of the reporter molecule selected, this assay enables convenient optimization of the required hydroxyl radical dose via attenuation of the beam or other approaches while at the beamline for a wide range of sample compositions. Our experience over the past decade for XF of soluble proteins using the MSH apparatus has shown that Alexa dose-response rates of 20–80 s^{-1} generally provide a useable level of labeling and coverage without excessive sample destruction. In our initial report of the Alexa488 assay, we screened several common buffers and buffer components for their effects (Gupta *et al.*, 2007). This work showed that inorganic salts or buffers such as phosphate, cacodylate or borate have minimal effect on the achieved dose, in line with their limited reactivity with hydroxyl radicals. Conversely, organic buffers such as HEPES, or commonly used buffer components such as glycerol or EDTA, exhibit a considerably greater 'quenching' effect. Indeed, at the concentrations commonly used for biological experiments, many of these compounds show deviations from apparent first-order kinetics in the dose-response curve with an initial lag phase followed by a sharp decay. This behavior can often be overcome by increasing X-ray flux and hence the total hydroxyl radicals available for reaction, which suggests differences in inherent reactivity towards OH radicals for Alexa488 compared with certain organic compounds.

Given the increasing interest of the research community in applying synchrotron XF to challenging problems such as membrane proteins or *in vivo* studies of protein/nucleic acid assembly that often have complex buffer compositions, the development of the 96-well high-throughput device offers a logical opportunity to develop an efficient screening pipeline to assess the effects of sample composition on hydroxyl radical dose, in order to facilitate experiment optimization by the XF user community. It became apparent early on in our screening effort that the handheld fluorimeter (Turner Biosystems TBS-380) previously used to measure Alexa488 fluorescence would greatly limit throughput and introduce additional error due to the need to manipulate and measure individual samples. To address this, we purchased a 96-well plate reader (BioTek Instruments Synergy H1M) for the XFP beamline sample preparation area. This instrument allows a direct readout of Alexa488 fluorescence from PCR plates, strips, and individual tubes both before and after exposure with no required sample manipulation as part of the footprinting workflow, with an entire PCR plate readout in under 60 s.

3.2. Survey of a library of organic buffer compounds

With the plate-reader setup in hand, we employed the new 96-well high-throughput endstation to revisit the role of buffer components and other molecules, with a goal of developing a greatly expanded reference library of compounds and their effects pertinent to the source characteristics and standard configuration of the XFP beamline. A set of 26 different organic compounds with various roles in biological sample preparation, including buffers, detergents, reducing agents and organic solvents, was selected. Alexa488 dose-response assays were performed at 25°C for each compound at 0, 10, 20 and 30 ms time points over a range of concentrations generated by serial dilution into phosphate-buffered saline (PBS) pH 7.4 buffer (composition: 137 m*M* NaCl, 2.7 m*M* KCl, 10 m*M* Na_2HPO_4, 1.8 m*M* KH_2PO_4). We selected a fixed attenuation of 305 µm of aluminium to provide an intermediate photon flux on the sample (Fig. S1 and Table S1); an Alexa488 dose-response rate of 180 s^{-1} was measured for PBS buffer under these conditions at an NSLS-II ring current of 400 mA using the 96-well HT device. Fig. 4 depicts the effect of concentration on the rate of radiolytic decay of Alexa488 for this compound library, organized by the role of the compound.

Synchrotron XF experiments are preferentially carried out using phosphate- or cacodylate-based buffers that show minimal hydroxyl radical quenching. Acceptable alternatives include citrate, ammonium acetate ($NH_4CH_3CO_2$) and sodium bicarbonate ($NaHCO_3$), all of which show only modest levels of quenching at the 5–20 m*M* concentrations often used in the laboratory [Fig. 4(*a*)]. Conversely, other common buffers such as tris [tris(hydroxymethyl)aminomethane], MES [2-(*N*-morpholino)ethanesulfonic acid] or HEPES [4-(2-hydroxyethyl)-1-piperazineethanesulfonic acid] [Fig. 4(*b*)] show significant quenching compared with PBS buffer, even at µ*M* concentrations. Indeed, Alexa decay rates could only be reliably determined for concentrations <5 m*M* under our conditions, a level at which buffering capacity is low and the system is increasingly susceptible to undesirable pH perturbation. For systems where non-preferred buffers such as HEPES must absolutely be used, a considerably higher flux density and thus radical dose is required, such as can be obtained at the High Dose Endstation of the XFP beamline using a capillary flow device (Asuru *et al.*, 2019).

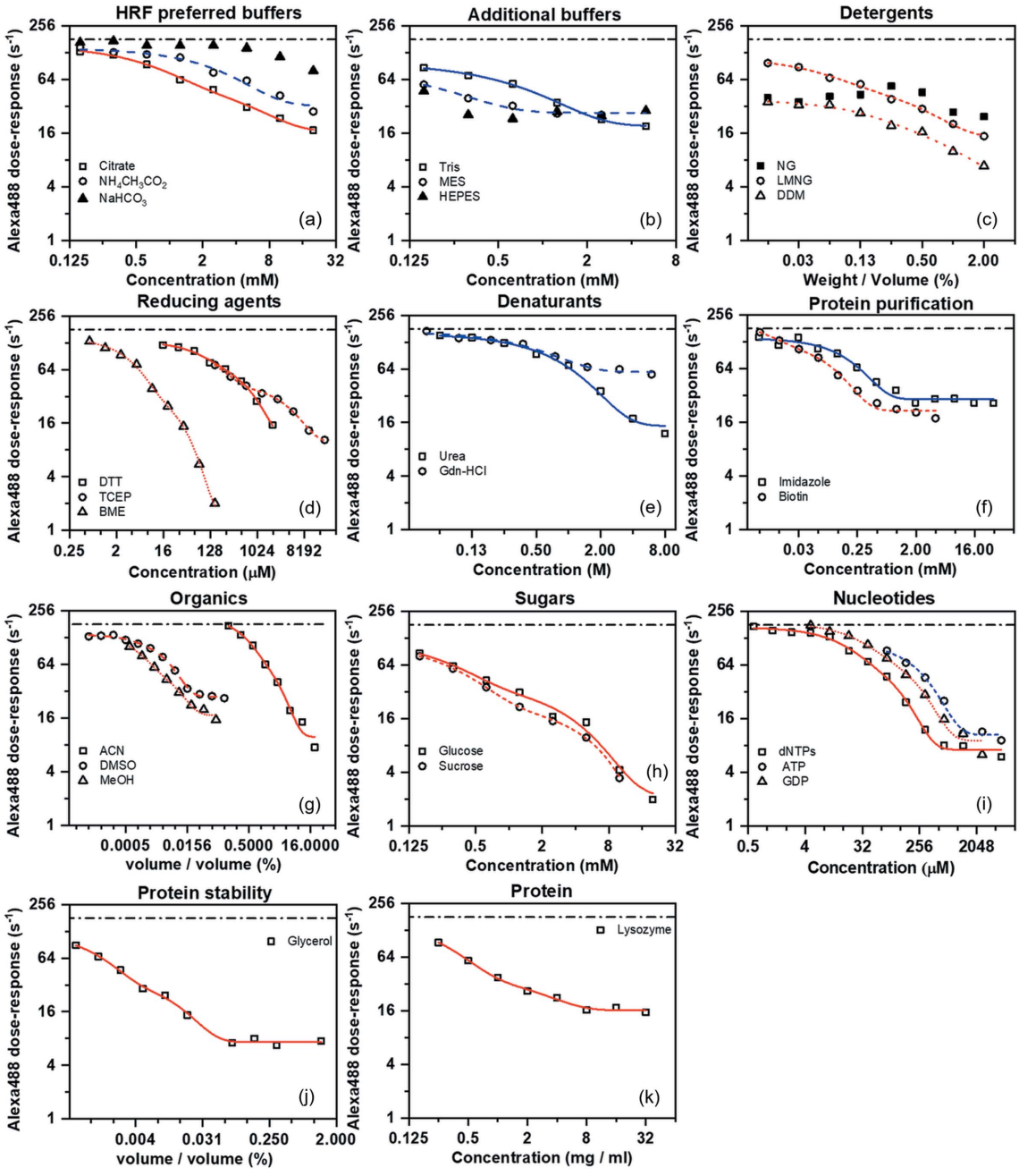

Figure 4
Plots of Alexa488 hydroxyl radical dose-response rates obtained for radiolytic degradation of 4.0 μ*M* Alexa488 in PBS pH 7.4 buffer versus concentration of buffer constituents and other organic compounds commonly used in studying biomolecules, organized by compound class. The lines show fits to either single or double exponential functions to highlight phase behavior (Table S2); some compounds (HEPES, $NaHCO_3$, NG) show poor fits to these functions over the concentration range studied and so their fit lines are not shown. A dot–dash line is shown to indicate the Alexa488 hydroxyl radical dose-response rate of 180 s^{-1} measured for PBS pH 7.4 buffer under the conditions used for this study. For the detergent experiment in (*c*) the concentrations span the typical concentrations employed for biomolecular purification, which typically are two to three times the critical micelle concentration (CMC); the CMC for the detergents studied: DDM [0.0087%(*w*/*v*)], LMNG [0.001%(*w*/*v*)] and NG [0.2%(*w*/*v*)]. Abbreviations/chemical names: $NH_4CH_3CO_2$, ammonium acetate; $NaHCO_3$, sodium bicarbonate; tris, tris(hydroxymethyl)aminomethane; MES, 2-(*N*-morpholino)ethanesulfonic acid; HEPES, 4-(2-hydroxyethyl)-1-piperazineethanesulfonic acid; NG, *n*-nonyl-β-D-glucopyranoside; LMNG, lauryl maltose-neopentyl glycol; DDM, *n*-dodecyl-β-D-maltopyranoside; DTT, dithiothreitol; TCEP, tris(2-carboxyethyl)phosphine; BME, β-mercaptoethanol; Gdn–HCl, guanidinium hydrochloride; ACN, acetonitrile; DMSO, dimethyl sulfoxide; MeOH, methanol; dNTP, deoxyribonucleotide triphosphate; ATP, adenosine triphosphate; and GDP, guanosine diphosphate.

A variety of reagents are used to maintain protein stability and solubility, including detergents that solubilize membrane proteins or hydrophobic drugs in aqueous solutions, as well as reducing agents that act to slow undesired oxidation of proteins, *e.g.* the formation of disulfide bridges. Both compound classes show marked quenching even at very low concentrations, compared with the PBS buffer baseline. Intriguingly, some detergents such as NG (*n*-nonyl-β-D-

glucopyranoside) show relatively invariant Alexa decay rates over concentrations spanning more than two orders of magnitude, while both LMNG (lauryl maltose-neopentyl glycol) and DDM (*n*-dodecyl-*β*-D-maltopyranoside) show increased quenching at higher concentrations [Fig. 4(*c*)]. The reducing agent *β*-mercaptoethanol (*β*ME) is a spectacularly effective quencher even at concentrations below 50 µ*M*, with dithiothreitol (DTT) being somewhat less reactive while TCEP [tris(2-carboxyethyl)phosphine] exhibits the least quenching and broadest usable concentration range [Fig. 4(*d*)]. The effective quenching by *β*ME and DTT is unsurprising given the high intrinsic reactivity of thiols towards hydroxyl radical oxidation. As a matter of good practice for synchrotron XF, detergent concentrations should be the minimum needed to maintain solubility and appropriately poise the biomolecule's state, and TCEP should be selected as a reducing agent over *β*ME or DTT.

We also examined the effects of compounds frequently involved in protein purification. Denaturants such as urea and guanidinium hydrochloride (Gdn–HCl) are used for protein-folding studies as well as purification of insoluble recombinant proteins. Both show only modest scavenging compared with most of the compounds evaluated in this study, although Gdn–HCl becomes an increasingly effective quencher at molar concentrations relative to urea [Fig. 4(*e*)], and so some care is warranted if protein folding is being investigated by footprinting methods. Imidazole and biotin, which are relevant to affinity-based purification methods using nickel or streptavidin affinity to an appropriately tagged protein construct, are effective quenchers even at sub-m*M* concentrations, showing a clear two-phase double-exponential curve that reaches a lower plateau at concentrations above 1 m*M* [Fig. 4(*f*)] under our conditions. In general, it is advisable to remove any imidazole or biotin present in samples purified by affinity-tag methods via buffer exchange or dialysis prior to synchrotron XF experiments to minimize this undesirable quenching.

Synchrotron XF has been successfully used to identify and probe small-molecule ligand-binding sites of protein targets at single amino acid resolution, making it a valuable tool for pharmaceutical drug discovery efforts (Kiselar & Chance, 2018). Dimethylsulfoxide (DMSO), which is frequently used as a solvent for drug ligand/fragment libraries, shows the strongest radical scavenging of any compound screened, with detectable quenching observed even at 0.001% (*v*/*v*) concentrations [Fig. 4(*g*)]. Acetonitrile may be a plausible alternative, as, while it shows a steep decrease in Alexa degradation rate as a function of concentration, it can be used at reasonably high concentrations of the order of 0.5% (*v*/*v*) with modest quenching under our conditions. We also found that sugars such as glucose and sucrose that are often found in protein-ligand studies are also effective quenchers, as shown in Fig. 4(*h*). Indeed, this result hints at the challenge of synchrotron XF of heavily glycosylated proteins using the more moderate flux density available for the 96-well HT device, as the carbohydrate sugars of post-translational glycosylation will provide effective competition for hydroxyl radicals [see Wang *et al.* (2010) for one successful XF study of a glycosylated HIV gp120 antigen protein]. Fig. 4(*i*) shows that nucleotides such as ATP (adenosine triphosphate) or GDP (guanosine diphosphate) are also effective radical scavengers even at high µ*M* concentrations. Protein XF studies of biological systems where these nucleotides are needed in the buffer preparation or act as substrates for enzymes of interest should be carefully designed to avoid excessively high nucleotide concentrations. Finally, the use of cryoprotectants such as glycerol for stabilizing samples also has a deleterious quenching effect that is clearly detectable even below 0.005% (*v*/*v*) [Fig. 4(*j*)] and should be avoided if at all possible for synchrotron XF experiments. This result is not unexpected given that glycerol is a sugar and has well known radical scavenging abilities in both protein crystallography (Allan *et al.*, 2013) and biological small-angle scattering (Crosas *et al.*, 2017).

We conclude our compound survey by highlighting the importance of considering the concentration of proteins being examined by footprinting methods. Most synchrotron XF experiments are carried out at protein concentrations of 5–10 µ*M* to provide sufficient samples for subsequent mass spectrometric analysis. As can be seen in Fig. 4(*k*) using chicken egg-white lysozyme (Sigma) as a model protein, significant hydroxyl radical scavenging by proteins is detectable at concentrations above 1 mg ml^{-1}. For proteins such as lysozyme (14.3 kDa) having modest molecular weights, 5–10 µ*M* concentrations in molarity units are readily achieved in <0.1 mg of protein per ml of buffer, where the level of quenching from the protein itself is modest. However, for larger proteins or protein complexes sized at hundreds of kDa or larger, or for studies of low-affinity protein complexes where one partner must be present in significant excess to saturate the binding site of the target protein of interest, the 5–10 µ*M* concentration optimum for MS will occur at concentrations well above 1 mg ml^{-1} where considerable scavenging can be expected. While the use of high-flux-density focused pink beam to produce a very high OH radical pulse represents one option to overcome this issue, the 96-well HT device described herein offers an attractive alternative using more modest X-ray flux densities, as it enables rapid exposure of a large quantity of samples at lower protein concentrations, which can then be pooled for subsequent mass spectrometric analysis.

3.3. Rapid OH dose optimization by tuning photon flux

The instrumentation we describe in this article enables rapid screening and optimization of the X-ray flux incident on the sample by remotely changing aluminium attenuator thickness with the attenuator wheel without needing to access the experimental hutch. The available attenuators are selected to provide a broad range of total photon fluxes (Fig. S1) and incident beam powers spanning 51 W with no attenuation to 3 W at 762 µm aluminium attenuation (Table S1), which permits hydroxyl radical dose optimization for a wide assort-

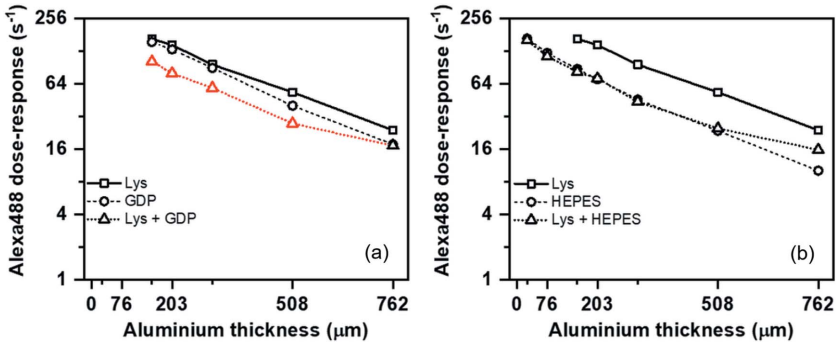

Figure 5
An illustration of experimental optimization by tuning aluminium attenuator thickness on the sample to vary X-ray flux on the sample (all the experiments were conducted at 400 mA NSLS-II ring current). The plots show Alexa488 hydroxyl radical dose-response rates obtained for 4.0 μ*M* Alexa488 in PBS pH 7.4 buffer for various attenuations as a function of various combinations of (*a*) 0.3 mg ml^{-1} of lysozyme and 80 μ*M* of GDP, and (*b*) 0.3 mg ml^{-1} of lysozyme and 160 μ*M* of HEPES.

ment of sample compositions. Fig. 5 illustrates this approach using chicken egg-white lysozyme as a model protein, with GDP and HEPES as representative organic compounds at fixed concentrations that could interact with protein or become scavenging components of the buffer. In a typical pairwise comparison by XF, Alexa488 dose-response measurements are performed separately for the target protein and its biomolecule binding partner or other ligand, to understand their respective hydroxyl radical quenching properties. Once reasonable OH radical doses are determined, Alexa screening is repeated for the protein in the presence of the biomolecule or ligand. As seen in Fig. 5(*a*), lysozyme and GDP show additive quenching over the full range of available attenuations, with several moderate attenuations (203, 305 and 508 μm) lying within the 20–80 s^{-1} optimum rate for good MS results. Conversely, with the more strongly quenching compound HEPES, there is no difference seen for HEPES alone and in the presence of lysozyme for almost all available attenuations [Fig. 5(*b*)]. This result indicates that HEPES has a limiting effect on the hydroxyl radical dose available to the protein for labeling at the concentration chosen. Furthermore, lower attenuations of 152 or 203 μm are required to provide the higher X-ray dose needed to overcome the scavenging effects of HEPES and achieve an Alexa488 decay rate optimum. Notably, each condition (protein, organic compound and organic compound in the presence of protein) shown here used a single 96-well PCR plate to screen up to eight attenuations at four different exposure times in triplicate; once the samples were prepared, the five conditions shown in Fig. 5 were exposed in ∼30 minutes using the 96-well high-throughput device with hutch access only required to swap PCR plates. This illustrates how our experiment optimization pipeline can quickly provide a comprehensive picture of the role of the entire sample composition and X-ray flux on hydroxyl radical dose, thus permitting increased attention to optimizing sample chemistry and selecting an ideal dose to provide high-quality exposed XF samples for detailed analysis by MS or sequencing methods.

3.4. Limitations of screening with Alexa488 fluorescence decay

While the loss of Alexa488 fluorescence with increasing X-ray dose provides a convenient spectroscopic handle with which to rapidly tune XF exposure conditions (Xu & Chance, 2007), it cannot substitute for the readout from MS or nucleic acid sequencing, both of which provide a true measure of solvent accessibility via changes in amino acid modification or nucleic acid backbone cleavage rates. Alexa488 is only a surrogate for these observables, as it merely tests for availability of X-ray radiolysis derived reagents that modify the Alexa488 molecule in bulk solvent. Furthermore, X-ray radiolysis of water generates solvated electrons in equal abundance to hydroxyl radicals. While these solvated electrons yield only modest damage to biological macromolecules, they may exert a more significant effect on the Alexa488 dye via electron capture that would alter its absorption spectrum and thus report fluorescence decay not pertinent to the biomolecule. The contribution of electrons to Alexa488 fluorescence decay could be accounted for by use of electron scavengers, although these reagents can also perturb radiolysis chemistry in other ways. For example, nitrous oxide (N_2O) reacts with solvated electrons to produce hydroxyl radicals that can then react with the Alexa488 dye or biomolecule; indeed, the use of saturated N_2O solutions has been reported to increase labeling coverage and efficiency in protein XF at low X-ray doses (Gupta *et al.*, 2014*a*).

3.5. Role of MS in synchrotron protein XF

MS analysis of exposed XF samples is an integral part of the protein XF experimental workflow. Typically, a 'bottom-up' proteomics approach is adopted in which samples are subjected to proteolysis to generate a set of unique peptide fragments, which are then separated and quantified using reverse-phase liquid chromatography (RP-LC) combined with MS. This approach allows covalently labeled peptides to be separated from unlabeled peptides by virtue of differing retention times in the RP-LC step, while permitting single-residue level characterization of the peptides through tandem mass spectrometry (MS–MS). In a typical two-state protein XF experiment, four different time points are measured for each state to generate a hydroxyl radical dose-response series, leading to a total of eight distinct RP-LC–MS experiments. A typical RP-LC–MS run for a single exposure time point of a medium-sized protein (∼40 kDa) uses a 90 min LC gradient, with at least two wash runs to clean the RP column between each time point. Consequently, a complete set of high-quality MS data for a two-state XF experiment may require up to a day of instrument time following exposure and proteolytic digestion. The MS data are then analyzed at the peptide level to uncover the extent of labeling on a global level across the

protein, followed by analysis down to the single-residue level of selected peptides to decipher dose-response changes and changes in solvent accessibly for single amino acids. This analysis typically requires several weeks of time for an experienced investigator to complete. Given these requirements, the identification of optimal XF exposure conditions while at the beamline represents a critical step in the synchrotron XF workflow, so that experimenter energies and MS resources are directed towards high-quality exposed samples yielding usable data. The instrumentation and experiment optimization pipeline described herein accelerates actual experimental work at the XFP beamline, with typically no more than a day of work needed at the beamline to carry out Alexa488 screening and subsequent XF exposures. More importantly, it provides a platform to greatly improve beamline-user productivity and synchrotron XF data quality by facilitating well optimized, reproducible and robust sample exposures, thus increasing the quality and utility of resultant MS data that can be used to assess structure and dynamics in a range of biological problems.

4. Summary and future plans

We have described the design of a new robust apparatus for high-throughput synchrotron XF based around a standard commonly used 96-well PCR plate format, as well as supporting instrumentation that enhances automation and monitors beam stability and component reliability at the XFP beamline. This platform facilitates screening and optimization of sample composition at the beamline, as demonstrated by an assessment of the influence of 26 different compounds commonly used in biological research. This characterization pipeline will help to facilitate synchrotron XF studies of biological materials in physiologically relevant media germane to the intracellular environment, as the influence of specific chemical components can be rapidly vetted.

Further improvements to XFP beamline resources for synchrotron XF are currently underway and are intended to enhance capabilities available to the user community ranging from experiment design to data analysis. For example, we are exploring the deployment of laboratory information management systems (LIMSs) such as *ISPyB* to synchrotron XF, building on the use of these database-driven resources at a number of macromolecular crystallography and biological small-angle X-ray scattering beamlines (Delagenière *et al.*, 2011; De Maria Antolinos *et al.*, 2015). Use of a LIMS for footprinting would allow collation of pertinent data about samples, the state of the beamline during experiments, and perhaps even subsequent MS or nucleic acid sequencing data analysis to be captured in one location, thus simplifying data and sample management for users and beamline staff alike. We are also working to make an MS instrument available at NSLS-II in a user-accessible sample preparation laboratory near the XFP beamline. This will provide a critically needed resource to validate and, if needed, adjust selected exposure conditions while carrying out XF experiments at the beamline, prior to investing in more extensive offline mass spectrometric data collection and analysis of exposed samples. This mass spectrometer will also provide a resource for training the structural biology community in XF data analysis, as well as access to MS data-collection resources for users lacking ready access to these instruments at their home institution.

Acknowledgements

We thank Dr Jen Bohon for her assistance with the development and testing of the first version of the 96-well apparatus. We also thank several members of the NSLS-II Data Science and Systems Integration Program for their assistance in deploying new capabilities as part of this project, including Jakub Wlodek for implementing and hands-on troubleshooting of the UVC *areaDetector* driver on the XFP beamline, Nathanael Maytan for implementing DIODE and developing the pulse-readout feature that enabled measurement of the Uniblitz shutter opening time, and Thomas Caswell for extensive assistance in developing *Bluesky* tools on the XFP beamline and prototyping an early version of the GUI. The US Government is authorized to reproduce and distribute reprints for government purposes notwithstanding any copyright notation thereon. The views and conclusions contained herein are those of the authors and should not be interpreted as necessarily representing the official policies or endorsements, either expressed or implied, of the Air Force Research Laboratory or the US Government.

Funding information

This work used resources of the National Synchrotron Light Source II, a US Department of Energy (DOE) Office of Science User Facility operated for the DOE Office of Science by Brookhaven National Laboratory under Contract No. DE-SC0012704. Funding for development of the XFP beamline was provided by a Major Research Instrumentation award from the National Science Foundation (DBI-1228549) and Case Western Reserve University. Operations support of the XFP beamline was sponsored by the National Institutes of Health (P30-EB-009998) and the Air Force Research Laboratory under agreement number FA8650-18-2-5402.

References

Allan, D., Caswell, T., Campbell, S. & Rakitin, M. (2019). *Synchrotron Radiat. News*, **32**(3), 19–22.
Allan, E. G., Kander, M. C., Carmichael, I. & Garman, E. F. (2013). *J. Synchrotron Rad.* **20**, 23–36.
Angel, T. E., Gupta, S., Jastrzebska, B., Palczewski, K. & Chance, M. R. (2009). *Proc. Natl Acad. Sci. USA*, **106**, 14367–14372.
Asuru, A., Farquhar, E. R., Sullivan, M., Abel, D., Toomey, J., Chance, M. R. & Bohon, J. (2019). *J. Synchrotron Rad.* **26**, 1388–1399.
Chance, M. R., Farquhar, E. R., Yang, S., Lodowski, D. T. & Kiselar, J. (2020). *J. Mol. Biol.* **432**, 2973–2984.
Clatterbuck Soper, S. F., Dator, R. P., Limbach, P. A. & Woodson, S. A. (2013). *Mol. Cell*, **52**, 506–516.
Crosas, E., Castellvi, A., Crespo, I., Fulla, D., Gil-Ortiz, F., Fuertes, G., Kamma-Lorger, C. S., Malfois, M., Aranda, M. A. G. & Juanhuix, J. (2017). *J. Synchrotron Rad.* **24**, 53–62.
Delagenière, S., Brenchereau, P., Launer, L., Ashton, A. W., Leal, R., Veyrier, S., Gabadinho, J., Gordon, E. J., Jones, S. D., Levik, K. E.,

McSweeney, S. M., Monaco, S., Nanao, M., Spruce, D., Svensson, O., Walsh, M. A. & Leonard, G. A. (2011). *Bioinformatics*, **27**, 3186–3192.

De Maria Antolinos, A., Pernot, P., Brennich, M. E., Kieffer, J., Bowler, M. W., Delageniere, S., Ohlsson, S., Malbet Monaco, S., Ashton, A., Franke, D., Svergun, D., McSweeney, S., Gordon, E. & Round, A. (2015). *Acta Cryst.* D**71**, 76–85.

Deperalta, G., Alvarez, M., Bechtel, C., Dong, K., McDonald, R. & Ling, V. (2013). *mAbs*, **5**, 86–101.

Du, Y., Duc, N. M., Rasmussen, S. G. F., Hilger, D., Kubiak, X., Wang, L., Bohon, J., Kim, H. R., Wegrecki, M., Asuru, A., Jeong, K. M., Lee, J., Chance, M. R., Lodowski, D. T., Kobilka, B. K. & Chung, K. Y. (2019). *Cell*, **177**, 1232–1242.e11.

Gupta, S., Celestre, R., Petzold, C. J., Chance, M. R. & Ralston, C. (2014*a*). *J. Synchrotron Rad.* **21**, 690–699.

Gupta, S., Chai, J., Cheng, J., D'Mello, R., Chance, M. R. & Fu, D. (2014*b*). *Nature*, **512**, 101–104.

Gupta, S., D'Mello, R. & Chance, M. R. (2012). *Proc. Natl Acad. Sci. USA*, **109**, 14882–14887.

Gupta, S., Sullivan, M., Toomey, J., Kiselar, J. & Chance, M. R. (2007). *J. Synchrotron Rad.* **14**, 233–243.

Hao, Y., Bohon, J., Hulscher, R., Rappé, M. C., Gupta, S., Adilakshmi, T. & Woodson, S. A. (2018). *Curr. Protoc. Nucleic Acid Chem.* **73**, e52.

Huang, W., Peng, Y., Kiselar, J., Zhao, X., Albaqami, A., Mendez, D., Chen, Y., Chakravarthy, S., Gupta, S., Ralston, C., Kao, H.-Y., Chance, M. R. & Yang, S. (2018). *Nat. Commun.* **9**, 3520.

Kiselar, J. & Chance, M. R. (2018). *Annu. Rev. Biophys.* **47**, 315–333.

Maytan, N. & Derbenev, A. A. (2021). In preparation.

Sangodkar, J., Perl, A., Tohme, R., Kiselar, J., Kastrinsky, D. B., Zaware, N., Izadmehr, S., Mazhar, S., Wiredja, D. D., O'Connor, C. M., Hoon, D., Dhawan, N. S., Schlatzer, D., Yao, S., Leonard, D., Borczuk, A. C., Gokulrangan, G., Wang, L., Svenson, E., Farrington, C. C., Yuan, E., Avelar, R. A., Stachnik, A., Smith, B., Gidwani, V., Giannini, H. M., McQuaid, D., McClinch, K., Wang, Z., Levine, A. C., Sears, R. C., Chen, E. Y., Duan, Q., Datt, M., Haider, S., Ma'ayan, A., DiFeo, A., Sharma, N., Galsky, M. D., Brautigan, D. L., Ioannou, Y. A., Xu, W., Chance, M. R., Ohlmeyer, M. & Narla, G. (2017). *J. Clin. Invest.* **127**, 2081–2090.

Sclavi, B., Sullivan, M., Chance, M. R., Brenowitz, M. & Woodson, S. A. (1998). *Science*, **279**, 1940–1943.

Wang, L., Qin, Y., Ilchenko, S., Bohon, J., Shi, W., Cho, M. W., Takamoto, K. & Chance, M. R. (2010). *Biochemistry*, **49**, 9032–9045.

Wlodek, J. & Gofron, K. J. (2019). *17th International Conference on Accelerator and Large Experimental Physics Control Systems (ICALEPCS'19)*, 5–11 October 2019, New York, USA, pp. 1492–1496.

Xie, B. & Sharp, J. S. (2015). *Anal. Chem.* **87**, 10719–10723.

Xu, G. & Chance, M. R. (2007). *Chem. Rev.* **107**, 3514–3543.